JATIS Journal of Astronomical Telescopes, Instruments, and Systems

RESEARCH PAPER

Characterization and evaluation of next-generation photon-counting image sensors for space applications

Nicholas R. Shade,[a,*] Gillian Kyne,[b] Shouleh Nikzad,[b,*] Edoardo Charbon,[c] and Eric R. Fossum[a]

[a]Dartmouth College, Thayer School of Engineering, Hanover, New Hampshire, United States
[b]California Institute of Technology, Jet Propulsion Laboratory, Pasadena, California, United States
[c]EPFL, Lausanne, Switzerland

ABSTRACT. Astronomers' pursuit of imaging light from increasingly faint and distant objects in the expanse of space necessitates continuous improvement in the signal-to-noise ratio of camera technology. Recent advancements in solid-state detector technologies have enabled the determination of photon number, including single-photon events, enabling observations at the fundamental limits of physics. We present an evaluation of three next-generation silicon-based detectors capable of photon-counting with deep-sub-electron input-referred read noise: the electron-multiplying charge-coupled device (EMCCD), the single-photon avalanche diode (SPAD), and the CMOS quanta image sensor (QIS). The EMCCD is built using a CCD sensor design that additionally employs repeated impact ionization to amplify the signal during readout, thereby reducing input-referred readout noise to deep-sub-electron levels and facilitating single-photon counting. SPAD devices utilize fast in-pixel signal amplification via impact ionization and positive feedback to achieve negligible effective read noise and precise time-of-arrival measurements of photons, enabling high-precision distance measurement and photon-counting. QIS devices take a distinct approach by utilizing a CMOS pixel topology that increases conversion gain without the need for impact ionization, thereby reducing readout noise to deep-sub-electron levels and enabling photon-number resolution, high dynamic range, and high spatial resolution. Characteristics of a representative device from each technology are evaluated with an emphasis on suitability for space flight missions. Furthermore, a summary analysis of emerging CCD and CMOS image sensors with "Skipper" readout for photon-number-resolving applications is also discussed in this report.

Keywords: CMOS image sensor; quanta image sensor; single-photon avalanche diode; electron-multiplying charge-coupled device; photon-counting; photon-number

Paper 25090SS received Mar. 12, 2025; revised Oct. 28, 2025; accepted Oct. 30, 2025; published Nov. 20, 2025.

1 Introduction: Photon-Counting Image Sensors for Astronomical Applications

The detection and imaging of light from faint and distant celestial sources remain central challenges in observational astronomy. Achieving high signal-to-noise ratios in imaging systems is critical for advancing the field, particularly in the ultraviolet (UV), visible, and near-infrared

*Address all correspondence to Nicholas R. Shade, nicholas.r.shade.th@dartmouth.edu; Shouleh Nikzad, shouleh.nikzad@jpl.nasa.gov

(NIR) spectral bands. Photon-counting image sensors have been a subject of research for several decades; however, only recently have solid-state photon-counting detectors become commercially and scientifically viable.[1] Next-generation sensors have been designed to detect individual photons, the fundamental particles or quanta of light, which allows for highly sensitive measurements that are crucial in astronomy. These advances in technology have led to significant improvements in the performance of photon-counting sensors, thereby enabling astronomers to observe phenomena that were once beyond the functional reach of traditional imaging methods.

A variety of photon-counting sensors have been developed, each with distinct characteristics that make them suitable for different aspects of astronomical observation. These sensors include vacuum-based technologies such as photomultiplier tubes (PMTs) and microchannel plates (MCPs); superconducting technologies operating at cryogenic temperatures such as nanowire single-photon detectors (SNSPDs), transition edge sensors (TES), and microwave kinetic inductance detectors (MKID); and silicon-based technologies such as electron-multiplying charge-coupled devices (EMCCDs), single-photon avalanche diodes (SPADs), and quanta image sensors (QISs).[2–4] Advancements in the readout signal chain have also shown potential in allowing photon-counting performance to be brought to more traditional silicon sensor topologies (CCD and CMOS) through multiple-sample-readout methodologies.[5–7] Due to each sensor's materials and architecture, they differ substantially in operational principles, temperatures, spectral range, and applications in which they can be used effectively.

This report aims to provide a descriptive and quantitative overview of the different types of silicon-based photon-counting sensors, focusing on their operational principles, performance characteristics, and applications in astronomy. Where possible, the report will compare sensor performance to the various technical requirements for future space flight missions. Notably, the current interest in creating large-format telescopes for ultraviolet (UV), visible, and NIR wavelengths, as outlined in the Astro2020 decadal survey. The decadal survey urges the development of new, highly sensitive, and efficient sensors that would enable the goals of the Habitable Worlds Observatory (HWO).[8] The Astro2020 decadal survey specifically set out for HWO to have "a versatility comparable to that of Hubble Space Telescope (HST) but an aperture comparable to James Webb Space Telescope (JWST), such an observatory would carry out groundbreaking observations of galaxy growth and address a majority of the science questions identified in the survey overall."[8] Given the scientific objectives of HWO, the likelihood of a photon-counting image sensor being needed and selected appears high. As such, an overview of various photon-counting image sensor systems will be provided; however, this report will be primarily focused on the silicon-based sensors (EMCCD, SPAD, and QIS) due to their significant recent advancements, their scalability and manufacturability, potential to achieve high resolution imaging, and ability to be easily enhanced for various wavelengths of sensitivity.[9,10]

To provide the most consistency in measurement techniques and conditions, we performed our own characterization of these next-generation photon-counting silicon-based sensors in a common laboratory environment whenever possible. We also cite prior studies when it was not possible to do our own measurements due to equipment availability, project scope, or cost. By understanding the capabilities and limitations of these sensors, it is hoped that their further development and future implementation will continue to advance astronomical research.

1.1 Applications for Astronomy

Silicon-based sensors have become increasingly integral to a variety of astronomical applications, owing to their ability to accurately detect photons, as evidenced by the 2009 Nobel Prize in Physics awarded for the invention of the CCD.[11] This and the new capability for photon-counting make them invaluable for deep-space observation, enabling high-resolution spectroscopy and facilitating the study of celestial events. More recently, time-domain astronomy has benefited from the precise timing capabilities of certain types of photon-counting sensors, allowing the study of transient events of supernovae, gamma ray bursts, and other rapid astrophysical events. In addition, the search for and characterization of exoplanets utilizes the sensitivity of photon-counting sensors to detect minute changes in starlight as planets transit their host stars or detect ultra-faint signals from the planet after starlight suppression.[12]

Table 1 presents key performance metrics for image sensors, highlighting their importance in various astronomical applications. However, it is often challenging to optimize image sensor

Table 1 Overview of important camera features.

Specification	Description	Importance
Resolution	Number of pixels in the sensor array	Higher resolution allows capturing more detail in celestial objects
Pixel size	Physical size of each pixel in micrometers	Smaller pixels can allow higher resolution, but larger pixels are better for low-light conditions
Quantum efficiency	Percentage of photons incident on the sensor that are converted into electrons	Higher quantum efficiency means better sensitivity to faint light from distant objects
Photon detection probability	Percentage of photons incident on the active part of the sensor that are converted to pulses and counted	It is used in single-photon detectors, whereas the detection of a photon is recorded as a digital signal. Higher photon detection probability means better sensitivity to faint light, similar to QE
Read noise	Input-referred noise generated by the camera's electronics when reading the signal	Lower read noise can improve the quality of images, especially in low-light conditions
Full-well capacity	Maximum number of electrons a pixel can hold before saturating	Higher capacity allows capturing brighter objects without saturation
Linear dynamic range	Ratio of the maximum to minimum measurable light signal within a linear regime	Higher dynamic range helps in capturing both very bright and very faint objects in the same image
Cooling	Requirement to cool the camera sensor to reduce thermal noise and improve the image	Cooling is crucial for long exposures needed in deep-sky astrophotography
Frame rate	Number of frames the camera can capture per second	Higher frame rates are important for capturing fast-moving objects such as planets
Light-collection duty cycle	The ratio of active integration time to total frame time, including readout, signal conversion, and conditioning	The duty cycle describes the efficiency of the light collection and how much time is lost to readout and signal processing
Bit depth	The number of bits used to meaningfully represent each pixel's intensity following analog-to-digital conversion	Higher bit depth allows capturing more subtle variations in light intensity and potentially higher dynamic range

performance across multiple criteria, as these metrics tend to compete with one another. As a result, astronomers and image sensor designers must prioritize sensor requirements based on specific scientific and experimental objectives.

To further illustrate the trade-offs inherent in sensor design, Table 2 outlines anticipated imaging requirements for instruments aboard the HWO mission, highlighting the importance of selecting the most suitable sensor for each objective. HWO precursor mission concepts such as Habitable Exoplanet observatory (HabEx) and Large UV Optical Near Infrared surveyor

Table 2 Sample Habitable Worlds Observatory camera anticipated needs.[13]

Instrument	Wavelength (nm)	Image sensor requirement description
Coronagraph system	900 to 2000	$<0.1e^-$ read noise, $<1 \times 10^{-4} e^-/p/s$ dark current, radiation hard
Near-UV/VIS detectors (NUV imager)	300 to 400	$>8K \times 8K$ pixels, $<2.5e^-$ read noise, $< 0.002e^-/p/s$ dark current, >50% QE between 300 and 400 nm
Far-UV detectors (UV spectrograph)	100 to 200	>40% QE 100 to 200 nm; 100 mm array size with 40 μm resels, 1×10^{-5} OOB rejection >300 nm

(LUVOIR) have similarly emphasized the need for matching image sensor capabilities to science applications.[14,15] Although imaging detectors have made significant progress in meeting the challenges of current space missions, no single technology can simultaneously address all technological requirements.

The scientific and engineering communities are constantly engaging in a dialogue to determine which sensor parameters are most critical for achieving specific Habitable Worlds Observatory mission objectives as well as all other future imaging mission objectives. The push for technological advancements must be balanced with consideration of technology readiness levels, as selecting the most advanced sensor may involve risks related to a lack of heritage and proven mission success. Legacy devices, on the other hand, provide a higher level of reliability and known performance, but they may not meet the demanding requirements of cutting-edge scientific missions.

1.2 Overview of Single-Photon Counting and Photon Number Resolving Sensors

The development of single-photon and photon number resolving imaging sensors has led to the availability of photon counting in various technology types. As the performance has improved, so have the definitions used to define these devices. Initially, reliable photon-counting sensors were defined as sensors that could achieve 0.3 e^-rms read noise.[16] However, subsequent analysis has determined that photon-counting performance peaks once read noise drops below 0.15 e^-rms.[17]

To achieve high sensitivity, most photon-counting sensors increase the signal-to-noise ratio by utilizing a high-gain mechanism that amplifies the signal generated by photoelectrons, thereby overcoming downstream readout noise and thus achieving deep-sub-electron input-referred read noise. However, each technology type uses a different method to achieve its high gain which leads each having unique performance benefits and drawbacks that affect the specific use case of each sensor. SPADs use Geiger-mode avalanche diodes to create digital pulses of photon arrivals, providing a simple and reliable method for photon detection at low jitter.[2] SNSPDs utilize cryogenically cooled nanowires to detect photon-induced changes in resistance, providing high detection efficiency and minimal timing jitter.[18] MKIDs operate by detecting changes in the kinetic inductance of superconducting resonators caused by incident photons, which can be measured to determine photon energy and arrival time.[19] TESs leverage the sharp change in resistance near the superconducting transition to detect single photons, offering high energy resolution and photon number resolving capabilities. EMCCDs are CCD detectors with an additional stage that creates a series of small amplifications via impact ionization to achieve a large overall gain. PMTs operate using photocathodes and a series of dynodes that create a cascade of an increasing number of electrons that can be easily detected. MCPs are closely related to PMTs but utilize a plate with numerous tiny channels that create an avalanching process allowing for small signal detection. CMOS-QIS sensors, which evolved from consumer and scientific CMOS image sensors, are the newest technology type and use novel low-capacitance, high-conversion-gain (V/e^-) pixels, to detect low-light levels.

In space imaging applications, each sensor type has valuable specialties. For instance, SNSPDs and TESs are used in astronomical observations, space-based LIDAR systems, and optical communications, providing high sensitivity and precision for detecting faint light from distant celestial objects. EMCCDs are employed in space telescopes and satellites for the detection and characterization of faint objects such as detection and characterization of exoplanets, spectrally resolved data gaining information about the life cycle of stars, formation and growth galaxies, surface and atmospheric characteristics of planets, and other astronomical phenomena. SPADs have been used for the development of *in situ* spectroscopy, such as time-resolved or gated Raman spectroscopy, enabling detection of Raman signals delineated from a fluorescence background which is used to investigate the chemical makeup of objects in space (and on Earth) such as organics to understand the habitability of a planet.

Research on the EMCCD, SPAD, and QIS devices has gained significant attention due to their high theoretical performance ceiling (e.g., sensitivity to visible photons, smaller pixels, and higher number of pixels), offering potential for significant advancements in various applications. These devices also function closest to traditional image sensors which allows greater flexibility in how they can be integrated into existing systems to easily create more capable

systems. In addition, as they are manufactured using well-known and well-studied silicon substrates and fabrication processes, they are compatible with processes such as delta doping and associated coatings processes which are agnostic to the pixel and readout architecture to enhance the sensor performance and for spectral tailoring.[9]

1.3 Operational Principles of Selected Silicon-Based Photon-Counting Sensors

The selected sensors, at the most fundamental operational level, utilize the photoelectric effect, where photons striking a photosensitive material can liberate electrons and holes in the form of charge carriers. These charge carriers (e.g., the electrons) are converted to a voltage and then processed into a digital signal. However, the method by which each sensor applies gain to the initial low-level signal varies significantly. The readout of the gained signal is also different for the different camera types.

1.3.1 *Operation and characteristics of EMCCD cameras*

EMCCDs are an enhancement of the traditional CCD. Traditional CCDs have a series of photosensitive and non-photosensitive gates that transfer charge in parallel to a series register that then goes to a single readout amplifier that converts the charge carriers to a voltage. Impact ionization gain over many stages was first developed in the 1990s by Hynecek at Texas Instruments as the Impactron, and the technology was further improved by Jerram at e2v as low-light imaging CCD (LLCCD).[20–22] These impact ionization-gain devices have come to be known as EMCCDs, and they operate by adding a high-field charge transfer section of the sensor where gain is repeatedly applied to the charge packets as they are transferred in a CCD register. In typical modern EMCCD designs, the multiplication register is incorporated before readout via the standard charge-to-voltage amplifier. In the multiplication register, the clocking voltage is dramatically increased from the standard operating clocking voltage to the order of 40 V, which creates a high electric field among clock phases over a short distance yielding a small probability of impact ionization, e.g., 0.01% per transfer as illustrated (and exaggerated) in Fig. 1. This results in a concomitant increase in the number of carriers when repeated over many transfer stages, and, with enough transfers through the multiplication register, a total large-scale amplification is possible. For example, a typical EMCCD might have an individual transfer gain probability of 0.012 and have 600 transfer stages which would result in a system gain of $\sim 1.012^{600} = 1283$.[24] Dark signal electrons are also multiplied in the transfer stages (it is useful to consider that in photon-counting applications, some pixels, prior to the multiplication register section, have a single photoelectron, some might have a single dark electron, and some have none). To reduce dark signal, an operating temperature of the order of -75 to -100°C is required.[25] Cooling an EMCCD can lead to a reduction in charge transfer efficiency (CTE) of the sensor. This leads to the need for an optimized and highly controlled operating regime, which results in the challenge of "tuning" the EMCCD operating voltage waveforms. Another drawback is that cosmic rays in the multiplication register can create blooming across an entire row.[26] Hot holes, which are also generated in the multiplication register, can lead to device aging.[27]

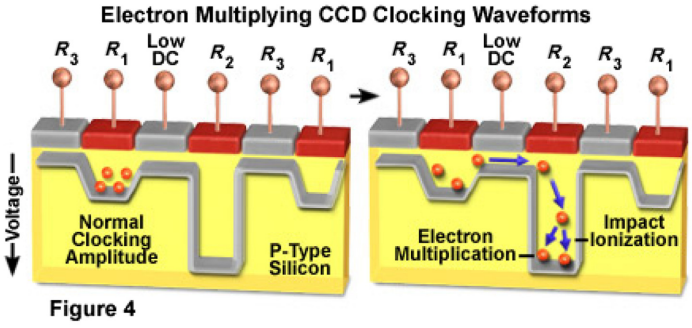

Fig. 1 EMCCD gain register consists of hundreds of specialized cells that amplify the signal via impact ionization, triggered by a carefully controlled and adjustable electric potential between the fixed-level gate and the high-voltage clocked gate.[23]

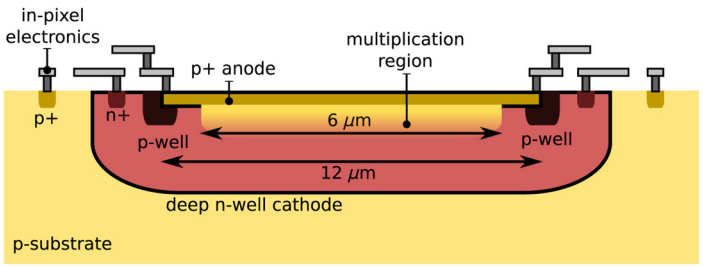

Fig. 2 Cross-section of the SPAD structure fabricated in a 0.35-μm high-voltage CMOS process. A p+ – deep n-well junction is used to create the multiplication region with a p-well guard ring to prevent premature edge breakdown.[28]

1.3.2 *Operation and characteristics of SPAD cameras*

SPAD cameras are semiconductor devices that operate in a high voltage mode above the breakdown threshold known as Geiger mode. When a photon is absorbed by the semiconductor, it generates an electron–hole pair (EHP). If this occurs in a multiplication region shown in Fig. 2, or one or both carriers diffuse to the multiplication region, the charge carriers (electron and/or hole) gain kinetic energy and travel in opposite directions. If a carrier with increased energy, above some threshold, interacts with the lattice, it may create additional electron–hole pairs via impact ionization.[29] As long as the original carrier and any additional electron–hole pairs remain in the high electric field region, they will then be re-energized and will further create additional charge carriers. This exponential growth process is known as avalanche multiplication and can include positive feedback if both types of carriers are involved because the electrons and holes travel in opposite directions. This multiplication process can result in a significant and measurable current pulse from a single absorbed photon. Due to the fast and high gain of avalanche multiplication, SPAD cameras can be used for precise timing measurements because they can read out a signal as soon as it arrives (as long as the photoelectron triggers avalanche multiplication, and it does not arrive during the dead time). This precise timestamping is compared with a traditional analog integrating sensor that has a fixed uncertainty in photon arrival timestamping because arrival could have happened any time during the integration window. For such traditional cameras, the typical way to reduce jitter and improve timestamp accuracy is to decrease integration time.

However, once a SPAD pixel is in active avalanche, additional photons will not create a measurable difference in the resultant signal level due to the presence of so many charge carriers from the avalanche process. This lack of sensitivity means subsequent photon arrivals after the triggering photon cannot be resolved during this period. The pixels need to be reset to sense new photons via a quenching of the avalanche multiplication. Quenching is an active or passive process that reduces the voltage across the SPAD which results in stopping, or "quenching," the multiplication process. The choice of active or passive quenching depends on speed, power, or complexity requirements. A significant limitation of SPAD cameras is the need for quenching and recharge, which introduces a dead-time period among perceived photon arrivals. This dead time lowers the light-collection duty cycle of the sensor and is a direct consequence of the device's inherent inability to handle new photons during the quenching/recharge period.[28] In addition, due to the need for quenching and recharge, or reset, electronics in the pixel, the fill factor of SPAD cameras may be lower than other CMOS technologies unless 3D stacking is used. Advanced SPAD cameras achieve fill factors in the order to 40% to 50%, depending on pixel-level complexity and pitch.[30] In addition, micro and meta-lenses can help mitigate the loss of photons due to fill-factor, achieving effective fill factors up to 80% in smaller SPAD pixels.

1.3.3 *Operation and characteristics of CMOS quanta image sensor cameras*

The QIS was originally conceived of as a sort of photon-counting binary image sensor with very small pixels and very high resolution that later morphed into multibit pixels that allow photon number resolution. At that time, SPAD pixels were too large to be considered for QIS application, but now, SPAD-QIS is being demonstrated with relatively small pixels and megapixel counts.[3] CMOS-QIS differ from conventional CMOS image sensors in terms of their novel CMOS pixel

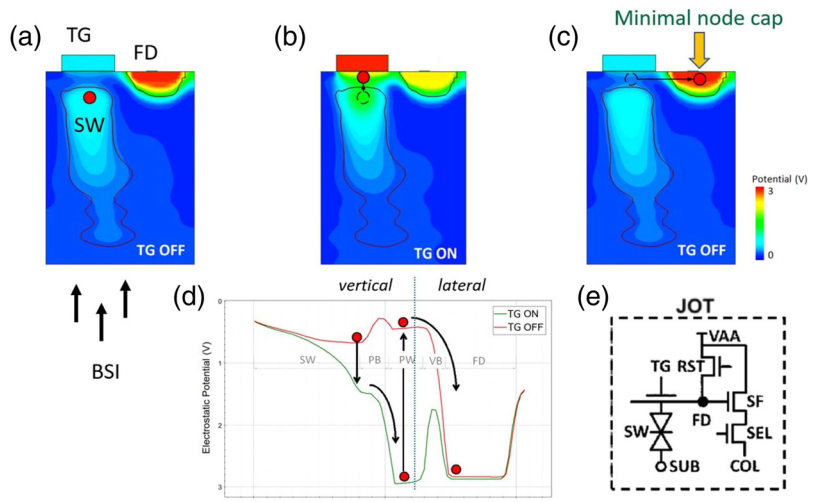

Fig. 3 (a)–(c) TCAD potential simulation of a pump-gate jot. The red circle represents the movement of a single photoelectron through the device. (d) Electrostatic potential curve along the charge transfer path. (e) Typical jot transistor structure.

topology. They were first reduced to practice at Dartmouth by designing a very high charge-to-voltage conversion gain pixel that utilizes tiny capacitors. Although it is possible to pair this capacitor design with a pinned-photodiode pixel (the typical pixel in current scientific CMOS image sensors), a vertically based backside-illuminated pixel with a buried storage-well was developed to achieve the design goal of a minimally small pixel size to realize billion-pixel sensors. To date, the highest resolution demonstrated by a Dartmouth spinoff company is 163 Mpixels with 1.1-μm pixel pitch.[3] This pixel design is called a "pump-gate jot" and is used to transfer the signal electron(s) to the ultra-low capacitance sense node for readout. The novelty of the pixel comes from the device's design which fully separates the floating diffusion node from the transfer gate, as seen in Fig. 3. The gap in elements eliminates the overlap capacitance which helps allow for such low capacitor values. Therefore, as the overlap was eliminated, the doping profile of the pixel was carefully engineered to allow full charge transfer across this gap by "pumping" charge vertically and then horizontally over this barrier.[31] The resulting capacitance from this new topology can be quite small which allows for very high conversion gain (e.g., 300 $\mu V/e^-$) and thus achieves signal amplification without the need for impact ionization and the associated high-voltage operation. These improvements allow QIS devices to work at room temperature with very low dark current and much lower power consumption than the other technologies.[32] A drawback of QIS devices pushing current lithography limits is the residual non-uniformity of the pixels and readout. The part of the non-uniformity that comes from the pixel is primarily due to conversion gain variance due to process variation which can be overcome with further development. The other source of signal non-uniformity is readout non-uniformity of the quantizer threshold voltage or analog-to-digital (ADC); however, there have been several proposals to mitigate this issue, and it is not fundamental.[33] However, as these photo response non-uniformities will be fixed over the lifetime of the device, simple flat field calibrations will be able to minimize any effect on science data.

1.3.4 *Operation and characteristics of Skipper-enabled cameras*

Recent research has explored the application of multi-sample-readout techniques as a viable alternative to developing unique pixel topologies to enhance the performance of standard CCDs and CMOS cameras.[34] One such technique is the "Skipper" readout, which incorporates principles similar to correlated multi-sampling (CMS), which is sometimes referenced as Fowler sampling.[35] Both Skipper readout and CMS readout involve many samplings of the reset and signal level that are subsequently averaged together. The difference is that CMS sequentially takes multiple samples of the reset level and then takes multiple samples of the signal level. The multiple samples of each respective signal level allow averaging to reduce the final noise in the signal. In the Skipper readout, the device uses a floating gate to nondestructively move the

signal charge back and forth between the sense node and a storage node many times and sample the signal at each transfer. Therefore, each sample of the reset and signal levels is independent events, but the noise between a reset and a sample is more highly correlated together than in the multiple samples of a CMS readout. "Chopping" the signal helps suppress $1/f$ noise and kTC noise. In the latter, Skipper readout uses multiple rounds of correlated double sampling (CDS) to suppress the kTC noise relative to the signal and thus improves imaging performance.[6] Performing these Skipper operations will take significant time and greatly diminish the light collection duty cycle of the camera. The exact number of skipping operations needed depends on the read noise of sensor in normal operations. For example, Ref. 7 reports a required 3025 samples to go from 11 e^- to 0.18 e^- read noise and operates at 118 K to reduce "contamination" from thermally generated carriers during the long readout process. Both CMS and Skipper readout have a negative impact on light-collection duty cycle. CMS readout is less significant due to its sequential sampling methodology. Skipper in comparison is much worse because it has to not only capture the same amount of samples, but it also has to perform the skipping transfer of charge to re-correlate each pair of samples. This leads to a sensor with a very poor duty cycle value that wastes precious device lifetime on signal processing. However, if the Skipper readout were to be applied to a QIS sensor that already has very low-read noise, the required number of Skipper samples would be much lower, and therefore, the skipping would have a much lower effect on the sensor duty cycle. A number of approaches for incorporating Skipper readout in CCD or CMOS formats are being pursued by a number of investigators including some of the authors.

2 Characterization Testing Outline

A comprehensive characterization plan was developed to evaluate the performance of three camera technologies: a QIS camera, an EMCCD camera, and a SPAD camera. This plan involved acquiring the necessary camera equipment from various collaborators and testing them on a unified apparatus at the NASA-JPL facilities. The NASA-JPL testing environment utilizes a vacuum-enabled UV/VIS monochromator setup which enabled the measurement of high-precision data at various wavelengths extending into the far UV spectrum. Standard photon transfer curve (PTC) graphs would be used as the baseline for traditional noise, conversion gain, and full-well analysis. As such, the conversion gain from the data is used to re-plot the PTC in terms of electrons to make the comparison of the charts more intuitive. The photon-counting histogram (PCH) also calculates read noise and conversion gain but based on a single photon flux measurement rather than a sweep of intensities. The PCH method is especially useful for its efficiency in testing variations across the whole image sensor by providing per-pixel performance characterization.[36] Quantum efficiency (QE) measures the whole camera system's performance by measuring photon detection effectiveness. The QE (or photon detection probability in SPAD sensors) curves would be taken across the visible and UV wavelength spectrum based on the PCH methodology. Finally, dark current (or dark count rate in the case of SPAD sensors) would be measured to help evaluate the need for cooling of the sensors and how long the cameras can integrate a single image before becoming too corrupted with spurious data.

Due to time limitations, the full characterization plan was not completed at the time of writing. The EMCCD data were collected at JPL with the prescribed testing setup. The QIS and SPAD cameras were primarily tested at Dartmouth with a different flat field light source, but the fundamental testing protocol was the same. The principal testing effort was focused on the QIS camera and thus was the most thoroughly assessed. The QIS results are especially important because the QIS devices are the least well-studied subset of the silicon-based sensors. The results for the EMCCD and SPAD camera were supplemented by prior published figures where data were available.

3 Results: Characterization of EMCCD, SPAD, and QIS

3.1 Characterization of the EMCCD Camera

The EMCCD investigated in this study was a Teledyne-e2v CCD201-20, a 1k × 1k format frame-transfer sensor with 13-μm square pixels.[37] This sensor had been processed with NASA-JPL's

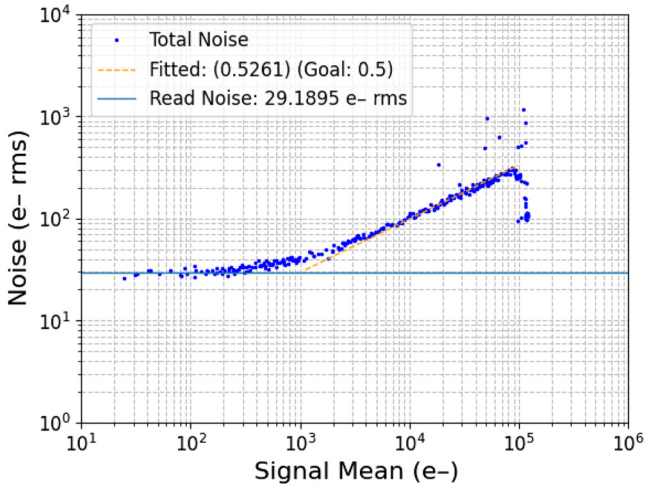

Fig. 4 Photon transfer curve of EMCCD camera without the high voltage gain with a 14.78 e^-/DN conversion gain. Taken at – 85°C with a constant 600-nm light source and the integration time as the variable.

delta doping technology, an advanced nanoscale surface engineering treatment that achieves near 100% internal quantum efficiency from soft X-ray to visible spectral range.[26,38–41] The net QE, which accounts for the fill factor, is crucial for comparing the signal-to-noise performance of different technologies. This is because higher QE can help offset other limitations, such as read noise, making it a critical factor for overall performance. Delta-doping technology described here is agnostic to the pixel architecture and is applicable to all silicon-based image sensors, including photon-counting sensors and those in this study. As such, QE does not feature as a means for comparison in this study; however, QE comparison remains an important metric in comparison with non-silicon-based sensors.

As described in Sec. 1.3, the architecture of the EMCCD allows operation with or without EM gain with user-selectable values. Typically, operation is separated into one of three operating modes; unity gain mode where the device behaves as a normal CCD, "analog mode" where EM gain is applied to reduce the effective read noise of the device as the expense of the excess noise factor, and "photon counting" (PC) mode whereby operation with low flux (typically $\leq$0.1 counts/pix/frame), high gain (typically $\geq$1000) combined with thresholding eliminates read noise and gives the ability to count individual photons.

CCD and analog mode were investigated in this study to demonstrate the principle of a reduced "effective" read noise. Figure 4 shows a photon transfer curve obtained in unity gain mode at 1 MHz serial clocking speed, where the fitted shot noise slope was used to derive a conversion gain of 14.78 e^-/DN. Unity gain read noise through the EM output of the device was calculated at 29 e^- and full-well capacity of $\sim$80 ke^-.

A PTC produced by utilizing an EM gain of approximately $\times$6000 is shown in Fig. 5. The expected shot noise slope is preserved; however, the EM gain has the effect of reducing the maximum effective image area full-well capacity by a factor approximately equal to the register full-well capacity divided by the applied gain. In this case, the full-well was limited to $\sim$40 e^-. The effective read noise is given by the unity gain read noise divided by the applied EM gain, $\sim$0.006 e^- in this case, and so well within the photon-counting regime; however, the excess noise factor and dark signal/clock-induced charge now require consideration for total signal/noise performance. The excess noise factor equates to an effective halving of the detector's quantum efficiency and so provides a benefit only when the flux level is approximately equal to or below the system read noise.[42] Operation in photon counting mode is preferred because this eliminates the excess noise factor; however, a fraction of photons is always lost beneath the chosen threshold resulting in an effective hit to the detective quantum efficiency of the device.[43–45] It is typical to operate with an EM gain equal to $\sim$50$\times$ the read noise, giving a detective quantum efficiency of 90%. The incident flux must be kept below $\sim$0.2 counts/frame to avoid excessive coincidence events, and so operating with high frame rates is an effective strategy to maximize the regime where photon counting mode is applied.[43–45] Dark signal and clock-induced charge are then the

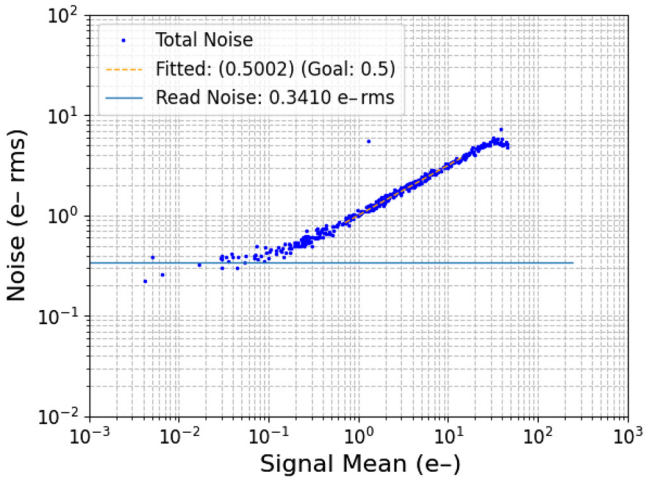

Fig. 5 Photon transfer curve for the EMCCD with the EM gain active with a 0.00242 e^-/DN conversion gain. Taken at – 85°C with a constant 600-nm light and the integration time as the variable.

primary noise sources, with dark signal as low as 0.05 e^-/pix/h possible with cooling to 168 K and clock-induced charge values ranging from 10^{-2} to 10^{-3} depending on the device and "waveform tuning" for the specific application.[26,46]

This characterization shows the utility of the EMCCD for flexible operations ranging from unity gain to the high gain mode. However, it also showcases the drawbacks in terms of the excess noise factor in analog mode, limited regime applicable to photon counting mode, and the inability to resolve the individual number of photons unlike low-noise CMOS and Skipper technologies.

3.2 Characterization of the SPAD Camera

The performance of SPAD cameras is typically evaluated using photon detection probability (PDP), which considers both "the photon transmission and the avalanche triggering."[47] It does not include the fill factor of the SPAD device which for most state-of-the-art devices continues to be a limiting factor with a fill factor of ~40% to 50%. As mentioned earlier, the PDP plots the detection probability of photons against the incident photon flux. The PDP of the SwissSPAD2 camera from EPFL is reproduced in Fig. 6.[48] The camera exhibits good performance, despite not having microlenses or other surface enhancements. Further planned tests with NASA-JPL's custom surface treatments will provide valuable insight into how well performance can be improved.

Due to the nature of SPAD cameras, the dark count rate (DCR) is used instead of dark current. Both metrics use the same units of electrons per second, but DCR is a more appropriate description for SPAD cameras due to their dead-time period where measurement information is lost. Figure 7 shows the dark count rate of the SPAD camera for various operating conditions. In

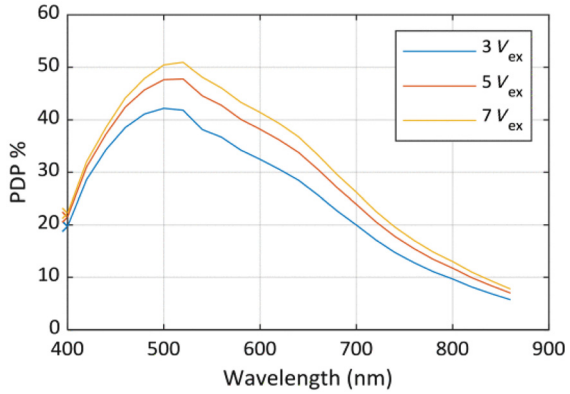

Fig. 6 PDP with the SPAD camera.[48]

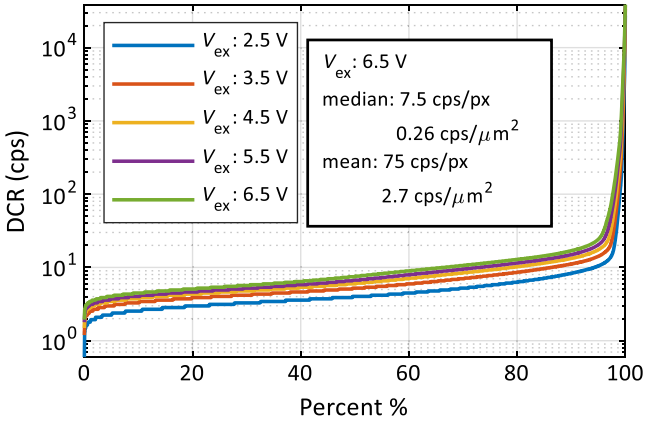

Fig. 7 Cumulative distribution of the dark count rate of the SPAD camera at 25°C.[48]

addition, temperature has an effect on the DCR of the SPAD. Lowering the temperature improves the DCR performance; however, it has minimal impact on the after-pulsing probability of the SPAD cameras.[49]

A comparison of Figs. 6 and 7 highlights an important characteristic of SPAD cameras: the excess bias voltage or overvoltage is a tunable parameter that affects both the PDP and DCR. Although increasing overvoltage can improve the PDP, it simultaneously degrades the DCR. Therefore, the overvoltage needs to be optimized based on the specific operating requirements to achieve an acceptable balance between PDP and DCR. Increasing PDP increases the likelihood of a photon being received overall, but a high DCR will block and influence photon-counting ability due to the effective 1-bit nature of a SPAD pixel. Therefore, for timing-sensitive measurements, lower DCR is more important, so that the device reports less false positives, but for general low-light multi-bit images (especially transient event imaging) better PDP is desired to get a better image.

Although SPAD cameras are fundamentally a single-bit image sensor, the single-bit frames can be binned together to make a multibit image. Using the binned 8-bit images from the SPAD camera, a PTC can be created with the same method as a standard CMOS image sensor (CIS) camera.[50] Figures 8 and 9 present the preliminary data from a standard PTC that was performed with the SPAD camera. Figure 8 shows the PTC curve of the SPAD camera with good success and shows a conversion gain of 0.992 e^-/DN (or 1.008 DN/e^-) in the linear region. It is also believed to be one of the first published results of a SPAD PTC in the typical PTC format. Due to its 1-bit frame capture design, many 1-bit frames are combined to make a single 8-bit image and thus referred to as a SPAD-QIS. The integration time of each 1-bit frame is constant at

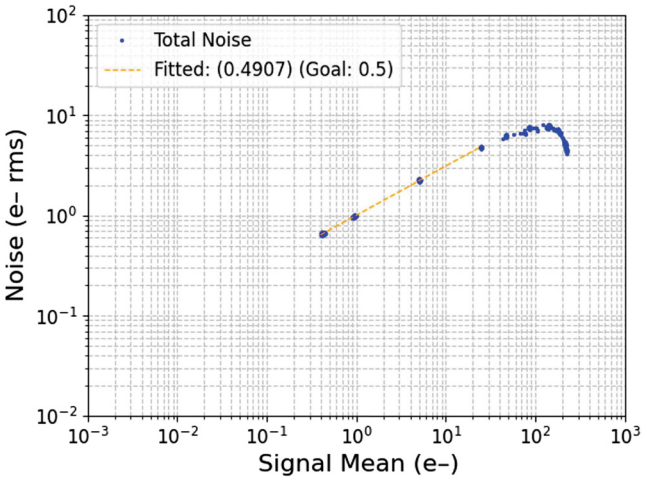

Fig. 8 Photon transfer curve of SPAD camera. Taken at 20°C with a constant 525-nm light source, constant integration time, and variable frame combination number. 0.992 e^-/DN conversion gain.

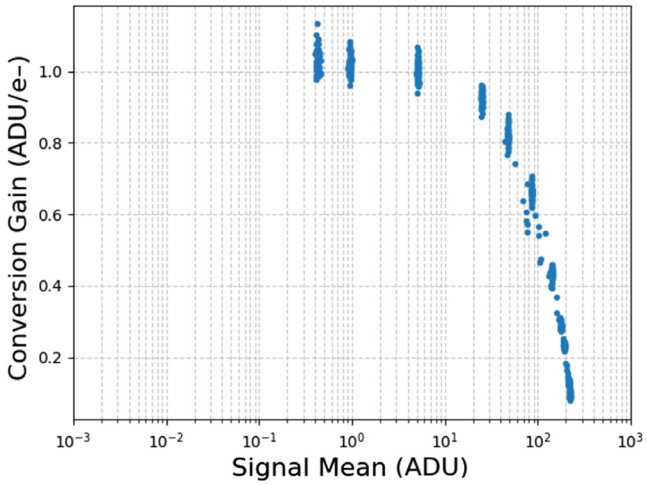

Fig. 9 Gain of the SPAD camera from the photon transfer curve data. Taken at 20°C with a constant 525-nm light source, constant integration time, and variable frame combination number.

22.8 ns with the independent variable being how many of those frames are used in each image combination. The choice of an 8-bit image was made due to the development camera having the native ability to perform and output the 8-bit bracketing. However, this reconstruction methodology is not limited to only 8 bits. The image bracketing can be extended to any arbitrary bit depth via on or off device post-processing, thereby enhancing the platform's design flexibility. Overall, the graph shows the expected PTC behavior of being shot noise limited until the standard deviation peaks and rolls off. Due to the effective full-well of the pixels being 1 e^-, the roll-off is due to the ADC reaching capacity due to the maximum data size of 8 bits. Figure 9 shows the gain of the SPAD camera throughout the capture series. The graph indicates the gain is ~1 DN per e^- for low light levels in the linear region; however, as illumination increases, the gain of the system decreases until the system reaches the ADC saturation limit. This is the standard occurrence for all cameras as they approach the full-well of the pixel or ADC.

3.3 Characterization of the QIS Camera

The primary QIS camera evaluated is an early Gigajot engineering-grade camera based on very early QIS devices made at Dartmouth, and it does not reflect the performance of later-generation cameras, which were not available to us for this work.[51] From a user perspective, it operates similarly to a traditional CMOS camera but with much improved performance. The standard testing operation of the camera utilizes active cooling to regulate the sensor temperature to 10°C. The camera was programmed to use eight CMS cycles. The sensor has 1024 by 1024 pixels which were all used for characterization of the sensor.

A standard PTC graph of the camera is shown in Fig. 10, plotted with a calculated gain of 0.0781 e^-/DN (or 12.81 DN/e^-). The graph was captured using 15 steps of integration time from 0.45 to 4852.18 ms (the minimum to the maximum integration time) with a 300-nm light source. The resulting plot exhibits the noise floor of the sensor on the left portion of the graph before becoming very linear in the shot noise-limited region, as expected. Due to limitations of the light source and developmental camera, there is a slightly extended gap in the data from 0.1 to 1.0 e^-; however, being an artifact of the testing setup, this does not affect the validity of the data.

Figure 11 shows an example of the PCH calculation for a single pixel. The blue area represents the raw data histogram, and the red line represents the PCH algorithmic analysis of the plot. By fitting a smoothing spline to the raw histogram, the peak and valley values can be extracted. The larger the difference between the peaks and valleys, the lower the read noise. Although the separation among peaks is representative of the conversion gain. The PCH testing setup uses LEDs that are shown into one port of an integrating sphere. The output of the integrating sphere then goes through a 20-m FWHM band pass filter at the corresponding wavelength. The flat field light illuminates the image sensor without a lens. A total of 5000 frames were captured for analysis as described in Ref. 36.

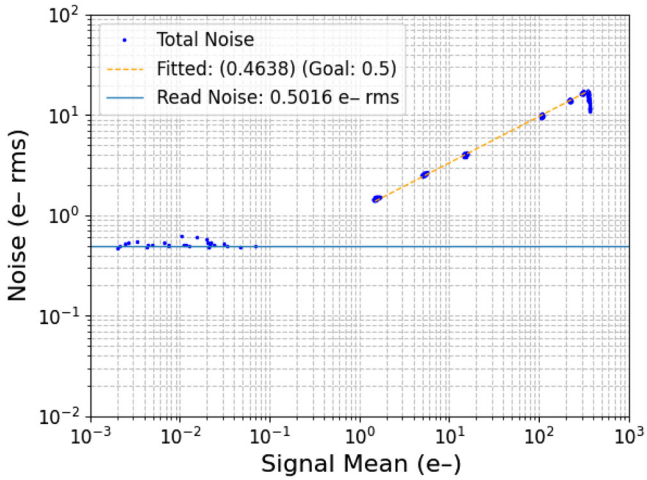

Fig. 10 Photon transfer curve of QIS camera. Taken at 10°C with a constant 300-nm light source and the integration time as the variable. [1 ADU = 0.0781 e^-].

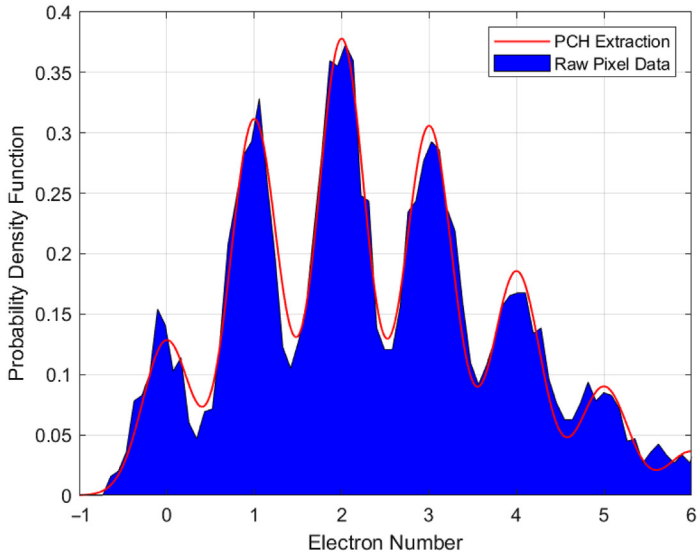

Fig. 11 Photon-counting histogram analysis chart of the QIS camera for a single pixel. Fitted red curve is for a read noise value of 0.275 e^- rms, a pixel conversion gain (CG) of 262.6 $\mu V/e^-$, and an average quanta exposure of 2.43 photons/frame. Many more grabbed frames of data would likely result in a smoother PCH, as seen in Ref. 51.

The non-uniformity of this very early QIS camera is one of its limitations, which can be seen in Figs. 12 and 13. Figure 12 shows the per-pixel noise on the left and the per-pixel conversion gain distribution on the right. The pixel-to-pixel variation in noise performance is most likely due to 1/*f* noise in the source follower and conversion gain variation; however, the median value of the distribution is 0.324 e^-, which is nearly sufficient for reliable photon-counting. The conversion gain is relatively high with a median value of 273 $\mu V/e^-$. Figure 13 shows the relationship between conversion gain (CG) and read noise in a heat map. The color coding is for the number of pixels bound by the small boxes on the plot. The figure shows that the majority of the pixels are well clustered in a deep sub-electron read noise (DSERN) area with the highest number of pixels clustered in the 267.5- to 272.5-$\mu V/e^-$ and 87.5- to 92.5-μVrms area. The diagonal trends in the graph are a function of the relationship between CG and read noise. The main limitation of the PCH analysis method is how the algorithm only functions well for DSERN pixels. As the noise approaches 0.5 e^- rms, the algorithm starts to break down. This is why work has been done to create algorithms that work well for DSERN and non-DSERN pixels simultaneously such as the PCH-EM algorithm.[52]

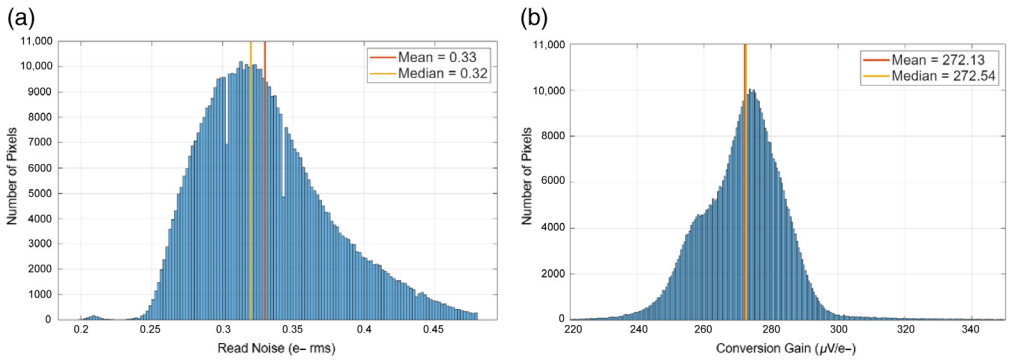

Fig. 12 Results of the photon-counting histogram algorithm for the QIS camera at 550 nm. (a) Graph of the individual pixel noise values. (b) Graph of the per-pixel conversion gain values.

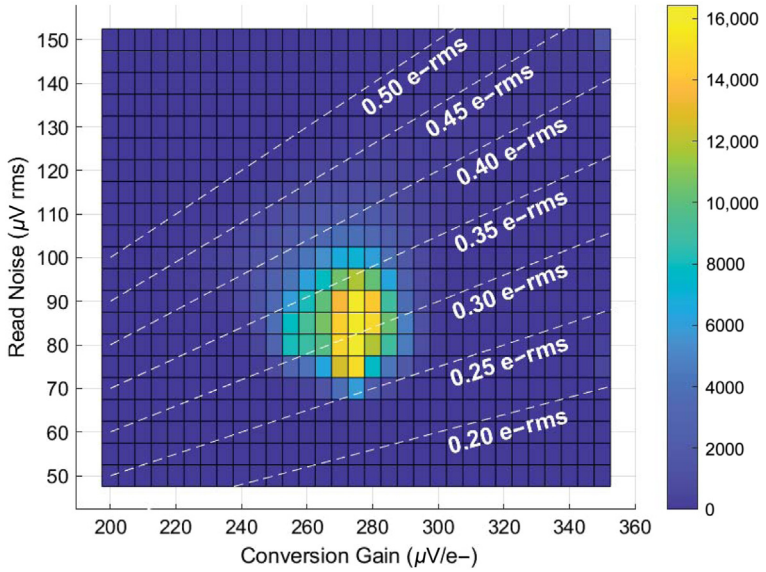

Fig. 13 Read noise versus the conversion gain for the QIS camera based on the photon counting histogram algorithm. The box color represents the number of pixels with the corresponding conversion gain and read noise.

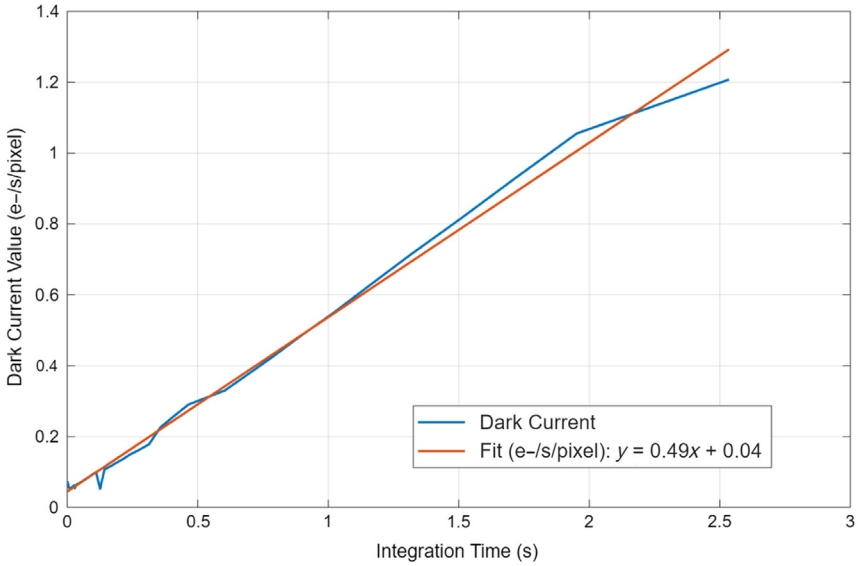

Fig. 14 QIS dark current based on an average of the whole image frame at various integration times. Taken at 20°C.

The dark current analysis graph is shown in Fig. 14. Using 50 logarithmic steps from the shortest (64 μs) to the longest (2.5 s) integration time, 25 frames of data were collected at each step. The mean pixel value at each integration time was calculated and plotted against integration time. Taking the slope of the resulting plot yields the dark current value for the camera. The resulting plot is very linear, which is expected, and has a slope of 0.425 e^-/s.

Figure 15 shows the histogram of the dark current of the QIS camera. In the figure, the variation of the pixels across the sensor is apparent. The peak of the dark current histogram is at 0.14 e^-/s, but the median value of the dark current is at 0.303 e^-/s due to the tail of the curve. Such a tail is common in nearly all semiconductor devices and may reflect a defect-energy and/or defect-density spatial distribution.

Figure 16 shows the spatial distribution of the dark current. In the graph, it is clear there are some defects along the corners of the camera. In addition, there are various types of noise present

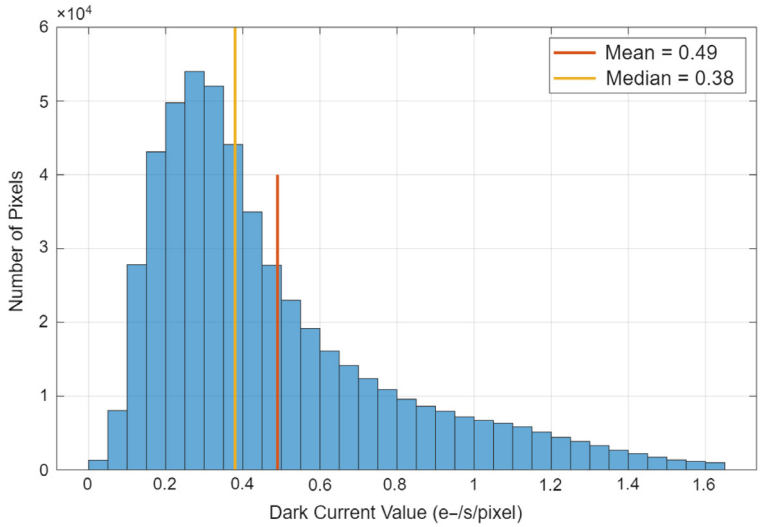

Fig. 15 Dark current histogram of the QIS camera at 20°C.

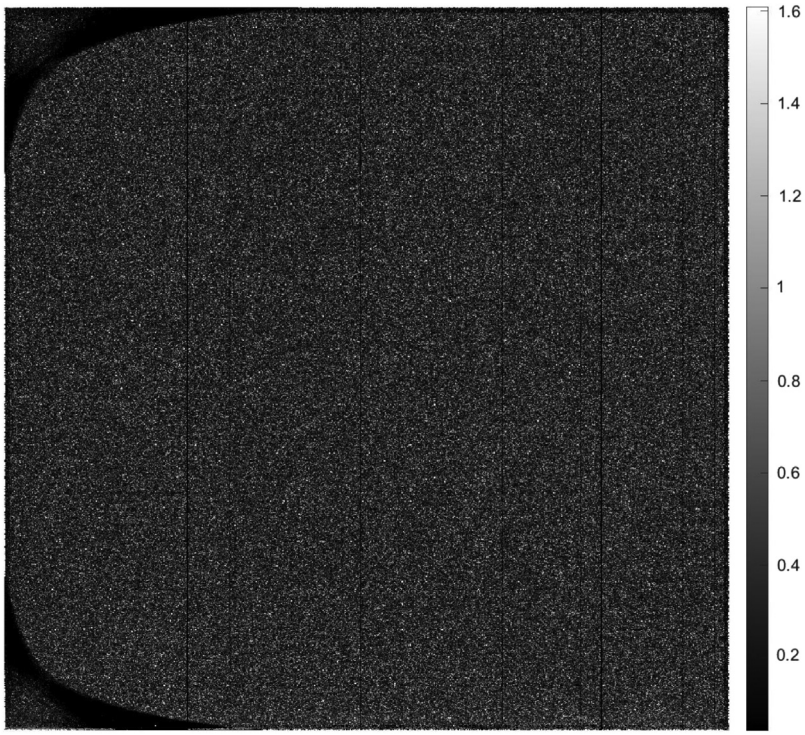

Fig. 16 Dark current (e^-/s/pixel) spatial distribution of an early QIS camera at 20°C.

in the columns in addition to some defective columns. Some of the noise is isolated and would be related to typical fixed pattern noise.

3.4 Silicon Detector Surface Enhancement

The QE performance of a detector is a complex function that is related to the semiconductor design and manufacturing, the coatings and backside treatment, and the optics on top of the sensor. For backside-illuminated silicon detectors, regardless of pixel architecture, 2D doping (encompassing delta-doping and superlattice doping) provides stable, reflection-limited response for silicon detectors. Coating design further allows scientists and engineers to selectively tailor the in- and out-of-band QE based on mission requirements.[53]

An example of wideband QE performance improvement that is achievable through backside processing is shown in Fig. 17, where backside enhancement was performed on a CIS120 from Teledyne-e2v (T-e2v).[10,54] In comparison, two examples of the tailorable nature of coating processes integrated with 2D-doped detectors are shown in Fig. 18. The left-hand graph was performed on a device with a five-layer anti-reflective coating. The results have been mission-enabling for the Faint Intergalactic Redshifted Emission Balloon experiment (FIREBall-2) and Star-Planet Activity Research CubeSat (SPARCS) missions.[56] In addition, the right-hand graph shows the ability to use their device agnostic processing to take a different sensor for a different

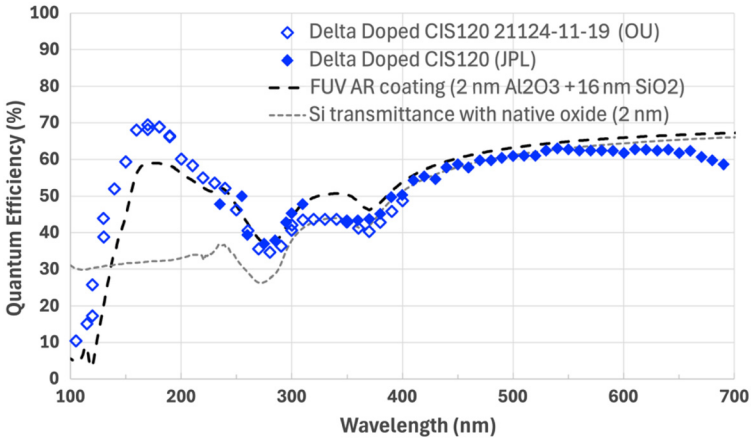

Fig. 17 QE of the 2D doped (delta doped) + AR coating CIS120 measured at the Open University and JPL. Jespar Skottfelta et al. Figure provided by M. E. Hoenk, JPL data produced by N. L. Bush.

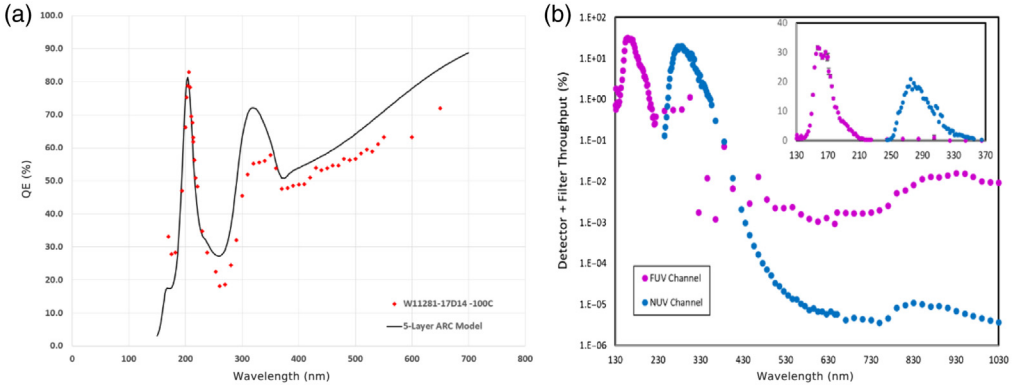

Fig. 18 (a) Quantum efficiency versus wavelength plot for a five-layer coating deposited on a thinned, delta-doped T-e2v CCD201-20 for the FIREBall-2 mission. The peak QE is 67.6% at 206 nm, and the data have been corrected using conversion gain measurements from photon transfer curves at each wavelength.[55] (b) Star-Planet Activity Research CubeSat (SPARCS) detector for both NUV (blue) and FUV (magenta) channels offers high in-band performance with several orders of magnitude out-of-band rejection.[56] All detector characterization was performed at JPL using a 1-m vacuum UV/VIS monochromator.

mission but still use the same general techniques and tailor its wavelength response to achieve the desired science objectives.[56]

4 Discussion: Comparison of Sensor Parameters and Future Testing Directions

The various parameters of the sensors, including their performance characteristics of power usage, and resolution, are summarized in Table 3.[57] Each camera has its unique merits and limitations which are not necessarily apparent from the empirical assessments. Notably, the total power usage and resolution of each camera vary significantly. In addition, it is important to note that pixel size and resolution requirement are dependent on observatory, telescope design, and instrument design. Currently, EMCCD, SPAD, and QIS can achieve a ~10-μm pixel size which is within the requirements of future large telescopes.[58]

Further testing is necessary to fully complete the performance characterization of these next-generation sensors. Radiation testing in particular is an essential parameter to evaluate, particularly for the QIS devices. Given the unique topology of QIS devices via the vertical nature of the small pixels in QIS devices raises concerns about their potential susceptibility to radiation damage. However, as the devices are fabricated using a standard CMOS process, there is potential for their radiation hardness to be similar to existing pinned photodiodes detectors.[59] Initial results from various groups indicate promising results that this is the case shown in Table 4.[60,61] Although these results are in line with current CIS image sensors, a continued and deliberate analysis into radiation-hard designs is required to fully validate these detectors for future space missions.[62]

Additional work could improve the performance of these cameras by incorporating Skipper readout or other novel readout techniques. As Ref. 5 explored in 1993 and recently demonstrated in Ref. 7, there is no fundamental reason to restrict Skipper readout to CCD camera technologies when it could be applied to traditional CMOS-based image sensors to enhance performance. Having a more precise readout methodology has the potential to relax requirements in other parts of the camera chip, leading to compounding levels of performance improvement.

Table 3 High-level summary of various photon-counting detector architectures (more work is underway for further comparisons of finer assignments of parameters for these technologies).

	EMCCD	SPAD	QIS
Single-photon sensitivity	Yes	Yes	Yes
Photon number resolution	Yes	No	Yes
Timing jitter	High (limited by readout architecture)	Lowest (<10 ps is possible)	Medium (limited by integration time design)
Dark current/dark count rate	Low	Low	Low
Pixel size	Small	Small	Smallest
Pixel resolution	High	Medium	Highest
Quantum efficiency	High (silicon surface treatments possible)	High (silicon surface treatments possible)	High (silicon surface treatments possible)
System power	High (due to mandatory cooling and EM gain circuitry)	High (due to fast electronics and avalanche circuits)	Low (CMOS-based, efficient design)
Manufacturability	High (mature CCD process)	High (CMOS-compatible, scalable)	High (CMOS-based, emerging but scalable)
Commercial availability	High (proven products readily available)	Medium (available but specialized)	Low (mostly in research phase)

Table 4 Preliminary radiation results of QIS cameras.

Institution	Pixel size (μm)	Radiation source	Radiation energy (MeV)	Radiation dose [krad(Si)]	Read noise pre-irradiation (e^- rms)	Read noise post-irradiation (e^- rms)	Dark current pre-irradiation (e^-/s/pix)	Dark current post-irradiation (e^-/s/pix)
ISAE-SUPAERO	4.6	Proton	60	30	0.36	0.44	0.018 @ 253 K	1.85 @ 253 K
ISAE-SUPAERO	4.6	Proton	60	30	0.37	0.41	0.014 @ 253 K	2.01 @ 253 K
ISAE-SUPAERO	4.6	Neutron	22	n/a	0.38	0.38	0.014 @ 253 K	2.62 @ 253 K
RIT	1.1	Proton	60	50	0.33	0.34	0.0063 @ 282 K	0.083 @ 286 K

In summary, we have performed a comparison of QIS, EMCCD, and SPAD cameras through characterization of typical performance metrics. QIS devices offer a potential path forward for photon-counting and photon number resolving applications in space. Their low power consumption, high resolution, low noise, and compatibility with advanced surface treatments such as 2D doping can make them attractive candidates for future missions. EMCCD detectors will be flying on the Roman Space Telescopes Coronagraph Instrument and have flown on suborbital missions such as FIREBall-2. With a known heritage and development pipeline, they provide a photon-counting option for future missions. SPAD cameras also have significant potential in future space flight missions. Although the principal goals of HWO do not align perfectly with the SPAD strengths, future SPAD detectors will be well-aligned with *in situ* instruments, e.g., Raman spectroscopy and time domain astronomy.

5 Conclusion: Possible Future of Astronomical Imaging

The future of discoveries in astrophysics will be in part enabled by innovative advancements in high-performance, photon-counting devices, and the next-generation silicon-based sensor technologies such as CMOS QIS, SPAD, and EMCCD cameras are perfectly poised to play a transformative role in those discoveries. They will have a high impact wherever they can meet photon-wavelength QE requirements due to the maturity of silicon and relatively easy scale up in resolution. We also note that 2D doping is agnostic to the pixel architecture and provides tailorable, stable, and high response in combination with custom coatings when applied to silicon image sensors and photon-counting detectors.

Overall, this report has presented a detailed evaluation of representative devices from each sensor class as part of a comprehensive assessment of these sensors, with a focus on their operational principles, performance metrics, and suitability for spaceflight applications. Through laboratory-based characterization and comparative analysis, the study has demonstrated the ability of QIS devices to achieve deep-sub-electron read noise and photon-number resolution with low power consumption and high spatial resolution; the continued relevance and performance of EMCCDs for low-light imaging and spectroscopic applications, particularly when enhanced with delta doping and optimized for UV sensitivity. In addition, the unique timing capabilities of SPADs make them well-suited for time-resolved and *in situ* spectroscopy applications. Finally, the integration of advanced readout techniques such as Skipper sampling and the application of 2D doping and tailored coatings have been shown to significantly enhance detector performance across all architectures and are subjects of ongoing investigations by some of the authors of this paper.

In conclusion, the continued development and integration of photon-counting sensors will be instrumental in enabling the ambitious scientific goals outlined in the Astro2020 Decadal Survey and beyond. These technologies will empower astronomers to probe deeper into the cosmos, detect fainter signals, and explore phenomena with unprecedented precision—ushering in a new era of discovery in astrophysics.

Disclosures

E.R. Fossum was a co-founder of Gigajot Technology, Inc., but no longer has a financial interest in the company. Edoardo Charbon was a co-founder of Fastree3D SA and Pi Imaging Technology SA, but he no longer has a financial interest in either company.

Code and Data Availability

The data reported on in this paper and the code used to process data are not publicly available at this time.

Acknowledgments

This work was in part supported by the National Science Foundation Research Traineeship, Transformative Research and Graduate Education in Sensor Science, Technology and Innovation (Grant No. DGE-2125733), and a Dartmouth PhD Innovation Program Fellowship. A portion of this research, including support of a JPL internship for N.S., was carried out at the Jet Propulsion Laboratory, California Institute of Technology, under a contract with the National Aeronautics and Space Administration (Grant No. 80NM0018D0004). This work expands upon the work presented and published in the SPIE Proceedings paper Ref. 63. The authors gratefully acknowledge helpful discussions with Drs. Nathan Bush and Michael Hoenk: Dr. Bush for providing feedback on the paper, especially on Sec. 3.1, and Dr. Hoenk for providing Fig. 17.

References

1. P. Seitz and A. J. P. Theuwissen, *Single-Photon Imaging*, Springer Science & Business Media (2011).
2. R. P. Mirin, S. W. Nam, and M. A. Itzler, "Single-photon and photon-number-resolving detectors," *IEEE Photonics J.* **4**, 629–632 (2012).
3. J. Ma, S. Chan, and E. R. Fossum, "Review of quanta image sensors for ultralow-light imaging," *IEEE Trans. Electron Devices* **69**, 2824–2839 (2022).
4. M. De Lucia et al., "Limitations to the energy resolution of single-photon sensitive microwave kinetic inductance detectors," *AIP Adv.* **13**, 125026 (2023).
5. E. R. Fossum, "Active pixel sensors: are CCDs dinosaurs?" *Proc. SPIE* **1900**, 2–14 (1993).
6. A. Suess et al., "Time domain noise analysis of oversampled CMOS image sensors," *IEEE Trans. Electron Devices* **69**, 2973–2978 (2022).
7. A. J. Lapi et al., "Skipper-in-CMOS: nondestructive readout with subelectron noise performance for pixel detectors," *IEEE Trans. Electron Devices* **71**, 6843–6849 (2024).
8. *Pathways to Discovery in Astronomy and Astrophysics for the 2020s*, National Academies Press, Washington, DC (2023).
9. S. Nikzad et al., "High performance silicon imaging arrays for cosmology, planetary sciences, & other applications," in *IEEE Int. Electron Devices Meeting*, pp. 10.7.1–10.7.4 (2014).
10. S. Nikzad et al., "High-efficiency UV/optical/NIR detectors for large aperture telescopes and UV explorer missions: development of and field observations with delta-doped arrays," *J. Astron. Telesc. Instrum. Syst.* **3**, 036002 (2017).
11. "The Nobel Prize in Physics 2009," NobelPrize.org, https://www.nobelprize.org/prizes/physics/2009/summary/ (2009).
12. P. Morrissey et al., "Flight photon counting camera development for the Roman Space Telescope coronagraph instrument," *Proc. SPIE* **12680**, 126800X (2023).
13. M. R. Bolcar and F. Zhao, *Habitable Worlds Observatory Technology Roadmap*, National Aeronautics and Space Administration, 14 Nov 2024, ntrs.nasa.gov/api/citations/20240014303/downloads/ExEP%20HWO%20TechWebinar_20241114_v2.pdf.
14. National Aeronautics and Space Administration, *The LUVIOR Final Report*, Goddard Space Flight Center, 26 Aug 2019, asd.gsfc.nasa.gov/luvoir/reports/LUVOIR_FinalReportAppendices_2019-08-26.pdf.
15. National Aeronautics and Space Administration, "HabEx Final Report," https://www.jpl.nasa.gov/habex/pdf/HabEx-Final-Report-Public-Release-LINKED-0924.pdf (2019).
16. N. Teranishi, "Required conditions for photon-counting image sensors," *IEEE Trans. Electron Devices* **59**, 2199–2205 (2012).
17. E. R. Fossum, "Modeling the performance of single-bit and multi-bit quanta image sensors," *IEEE J. Electron Devices Soc.* **1**, 166–174 (2013).
18. J. W. N. Los et al., "High-performance photon number resolving detectors for 850–950 nm wavelength range," *APL Photonics* **9**, 066101 (2024).
19. S. R. Meeker et al., "DARKNESS: a microwave kinetic inductance detector integral field spectrograph for high-contrast astronomy," *Publ. Astron. Soc. Pac.* **130**, 065001 (2018).

20. J. Hynecek, "CCM—a new low-noise charge carrier multiplier suitable for detection of charge in small pixel CCD image sensors," *IEEE Trans. Electron Devices* **39**, 1972–1975 (1992).
21. J. Hynecek, "Impactron—a new solid state image intensifier," *IEEE Trans. Electron Devices* **48**, 2238–2241 (2001).
22. P. Jerram et al., "The LLCCD: low-light imaging without the need for an intensifier," *Proc. SPIE* **4306**, 178–186 (2001).
23. T. J. Fellers and M. W. Davidson, "Concepts in digital imaging technology electron multiplying charge-coupled devices (EMCCDs)," Optical Microscopy Primer: Digital Imaging in Optical Microscopy, Molecular Expressions, 13 Nov 2015, micro.magnet.fsu.edu/primer/digitalimaging/concepts/emccds.html.
24. G. Martin and K. Cooke, *Understanding Electron Multiplying Gain*, Raptor Photonics, 17 Feb 2020, www.raptorphotonics.com/wp-content-uploads-2016-11-understanding-electron-multiplying-gain-pdf/.
25. K. B. W. Harpsøe, M. I. Andersen, and P. Kjægaard, "Bayesian photon counting with electron-multiplying charge coupled devices (EMCCDs)," *Astron. Astrophys.* **537**, A50 (2012).
26. G. Kyne et al., "Delta-doped electron-multiplying CCDs for FIREBall-2," *J. Astron. Telesc. Instrum. Syst.* **6**, 011007 (2020).
27. A. M. Evagora, "Factors affecting EMCCD technology for use in space," PQDT—Global, Open University (United Kingdom), England (2013).
28. S. Burri et al., "Architecture and applications of a high resolution gated SPAD image sensor," *Opt. Express* **22**, 17573–17589 (2014).
29. F. Capasso, "Physics of avalanche photodiodes," *Semicond. Semimet.* **22**, 1–172 (1985).
30. K. Morimoto and E. Charbon, "High fill-factor miniaturized SPAD arrays with a guard-ring-sharing technique," *Opt. Express* **28**, 13068–13080 (2020).
31. E. Fossum et al., "The quanta image sensor: every photon counts," *Sensors* **16**, 1260 (2016).
32. J. Ma and E. R. Fossum, "A pump-gate jot device with high conversion gain for a quanta image sensor," *IEEE J. Electron Devices Soc.* **3**, 73–77 (2015).
33. D. A. Starkey et al., "A novel threshold calibration methodology for quanta image sensors (QIS)," in *Proc. Int. Image Sensor Workshop (IISW)* (2019).
34. J. R. Janesick et al., "New advancements in charge-coupled device technology: subelectron noise and 4096 × 4096 pixel CCDs," *Proc. SPIE* **1242**, 223–237 (1990).
35. A. M. Fowler and I. Gatley, "Noise reduction strategy for hybrid IR focal-plane arrays," *Proc. SPIE* **1541**, 127–133 (1991).
36. D. A. Starkey and E. R. Fossum, "Determining conversion gain and read noise using a photon-counting histogram method for deep sub-electron read noise image sensors," *IEEE J. Electron Devices Soc.* **4**, 129–135 (2016).
37. Teledyne-e2v, "CCD201-20 BSI Datasheet (v11)," CCD201-20 Back-illuminated 2-Phase IMO Series Electron-multiplying CCD Sensor, https://www.teledynespaceimaging.com/en-us/Products_/Documents/ccd-datasheets/CCD201-20%20BSI%20Datasheet%20(v11).pdf (2025).
38. S. Nikzad et al., "Delta-doped CCDs for enhanced UV performance," *Proc. SPIE* **2278**, 138–146 (1994).
39. S. Nikzad et al., "Direct detection and imaging of low-energy electrons with delta-doped charge-coupled devices," *Appl. Phys. Lett.* **73**, 3417–3419 (1998).
40. M. E. Hoenk et al., "Delta-doped back-illuminated CMOS imaging arrays: progress and prospects," *Proc. SPIE* **7419**, 187–201 (2009).
41. S. Nikzad et al., "Delta-doped electron-multiplied CCD with absolute quantum efficiency over 50% in the near to far ultraviolet range for single photon counting applications," *Appl. Opt.* **51**, 365–369 (2012).
42. M. S. Robbins and B. J. Hadwen, "The noise performance of electron multiplying charge-coupled devices," *IEEE Trans. Electron Devices* **50**, 1227–1232 (2003).
43. O. Daigle et al., "CCCP: a CCD controller for counting photons," *Proc. SPIE* **7014**, 70146L (2008).
44. O. Daigle, P.-O. Quirion, and S. Lessard, "The darkest EMCCD ever," *Proc. SPIE* **7742**, 774203 (2010).
45. O. Daigle et al., "Characterization results of EMCCDs for extreme low-light imaging," *Proc. SPIE* **8453**, 845303 (2012).
46. N. L. Bush et al., "Assembly, optimization and calibration of the Roman coronagraph camera systems: the exoplanetary systems camera (EXCAM) and the low order wavefront sensing camera (LOCAM)," *J. Astron. Telesc. Instrum. Syst.* **11**, 31503 (2025).
47. A. Panglosse et al., "Modeling, simulation methods and characterization of photon detection probability in CMOS-SPAD," *Sensors* **21**, 5860 (2021).
48. A. C. Ulku et al., "A 512 × 512 SPAD image sensor with integrated gating for widefield FLIM," *IEEE J. Sel. Top. Quantum Electron.* **25**, 1–12 (2019).
49. M. Hofbauer, B. Steindl, and H. Zimmermann, "Temperature dependence of dark count rate and after pulsing of a single-photon avalanche diode with an integrated active quenching circuit in 0.35 μm CMOS," *J. Sens.* **2018**, 9585931 (2018).

50. I. M. Antolovic, C. Bruschini, and E. Charbon, "Dynamic range extension for photon counting arrays," *Opt. Express* **26**, 22234–22248 (2018).
51. J. Ma et al., "A 0.19e- rms read noise 16.7Mpixel stacked quanta image sensor with 1.1 μm-pitch backside illuminated pixels," *IEEE Electron Device Lett.* **42**, 891–894 (2021).
52. A. J. Hendrickson et al., "PCH-EM: a solution to information loss in the photon transfer method," *IEEE Trans. Electron Devices* **71**, 4781–4788 (2024).
53. A. D. Jewell et al., "Coatings and filters for ultraviolet imaging and spectroscopy," *J. Astron. Telesc. Instrum. Syst.* **11**, 042215 (2025).
54. J. Skottfelta et al., "Detector developments for UV space missions," *Proc. SPIE* **13625**, 136250P (2025).
55. E. T. Hamden et al., "Charge-coupled devices detectors with high quantum efficiency at UV wavelengths," *J. Astron. Telesc. Instrum. Syst.* **2**, 036003 (2016).
56. A. D. Jewell et al., "Performance of the SPARCS UV camera and detectors," *Proc. SPIE* **13093**, 1309304 (2024).
57. D. Robledo, "Photon-counting CMOS sensors extend frontiers in scientific imaging," https://www.photonics.com/Articles/Photon-Counting_CMOS_Sensors_Extend_Frontiers_in/a67740 (2022).
58. L. Buntic, D. F. Figer, and J. P. Gallagher, "Evaluating detector requirements for the next UV/O/IR flagship observatory," *Proc. SPIE* **12191**, 121911L (2022).
59. M.-L. Wu et al., "Radiation hardness study of single-photon avalanche diode for space and high energy physics applications," *Sensors* **22**, 2919 (2022).
60. J. P. Gallagher et al., "Radiation tolerance of a single-photon counting complementary metal-oxide semiconductor image sensor," *J. Astron. Telesc. Instrum. Syst.* **10**, 036003 (2024).
61. J. Krynski et al., "Radiation effects in quanta image sensors," *IEEE Trans. Nucl. Sci.* **72**, 1198–1207 (2025).
62. A. Antonsanti et al., "Ionizing radiation effects on hole collection backside-illuminated p-type deep-trench-pinned photo-MOS pixels under image acquisition," *IEEE Trans. Nucl. Sci.* **70**, 1958–1965 (2023).
63. N. R. Shade et al., "Characterization and validation of next generation image sensors for space applications," *Proc. SPIE* **13103**, 131030U (2024).

Nicholas R. Shade (student member) received his AB and BE degrees in electrical engineering from the Thayer School of Engineering, Dartmouth College, in 2020, where he is currently pursuing a PhD at Eric Fossum's Advanced Camera Technology Lab.

Gillian Kyne received her PhD at the National University of Ireland, Galway, in 2014. After completing a postdoctoral scholar at the California Institute of Technology, she joined the Advanced Detectors, Systems, and Nanoscience Team at NASA's Jet Propulsion Laboratory. She is the detector scientist for the FIREBall-2 balloon mission who led the characterization of the EMCCD noise and developed and delivered the camera to FIREBall-2 for its two flights in 2018 and 2022. Her general interests lie in detector development for space missions and ground-based observation.

Shouleh Nikzad is a JPL fellow, a senior research scientist, a principal engineer, and the head of the Science Division at NASA's Jet Propulsion Laboratory. In addition, she holds visiting faculty and lecturer appointments at the California Institute of Technology. Her research interests include materials and devices, detectors, instrument technologies, and instruments, especially in the ultraviolet/optical/near infrared part of the spectrum for space missions and terrestrial applications. Her recognitions include being an SPIE fellow, receiving the SPIE's Aden and Marjorie Meinel Technology Award, and most recently American Astronomical Society's Weber Award.

Edoardo Charbon received his diploma degree from ETH Zürich, Zürich, Switzerland, in 1988; his MS degree from the University of California at San Diego, La Jolla, California, United States, in 1991; and his PhD from the University of California at Berkeley, Berkeley, California, United States, in 1995, all in electrical engineering and EECS. Since 2002, he has been a faculty member with the École Polytechnique Fédérale de Lausanne (EPFL), Lausanne, Switzerland, where he is currently a full professor. He has been the driving force behind the creation of deep-submicrometer CMOS SPAD technology, which has been mass-producing since 2015 and is present in telemeters, proximity sensors, and medical diagnostics tools. He is a fellow of the Kavli Institute of Nanoscience, Delft. He was the chair of the VLSI Design. He is a distinguished visiting scholar of the W. M. Keck Institute for Space, Caltech, Pasadena, California, United States. He has authored or coauthored over 500 articles and 2 books, and he holds 30 patents. His interests span from 3D vision, LiDAR, FLIM, FCS, and NIROT to super-resolution microscopy, time-resolved Raman spectroscopy, cryo-CMOS circuits, and systems for quantum computing.

Eric R. Fossum is the John H. Krehbiel Sr. Professor for Emerging Technologies with the Thayer School of Engineering, Dartmouth College and Vice Provost for Entrepreneurship and Technology Transfer. He invented and developed the CMOS image sensor with intra-pixel charge transfer used in billions of smartphones and other applications each year and invented and developed the quanta image sensor. Major honors include the Queen Elizabeth Prize for Engineering, the National Medal of Technology and Innovation, the IEEE Andrew Grove Award, the OSA/IS&T Land Medal, and a Technical Emmy Award. He was the co-founder and the first president of the International Image Sensor Society. He was inducted into the National Inventors Hall of Fame and is a member of the National Academy of Engineering.